El Niño–Southern Oscillation extrema in the Holocene and Last Glacial Maximum

Athanasios Koutavas[1,2,3] and Stephan Joanides[4,5]

[1]   The El Niño–Southern Oscillation (ENSO) is the largest engine of interannual climate variability on the planet, yet its past behavior and potential for future change are poorly understood and vigorously contested. Reconstructions of past ENSO are indispensable for testing climate models tasked with predicting future ENSO activity in a warming world, but suitable geologic archives are scarce, especially for the last glacial period. Here we reconstruct mean climate and ENSO variability in the Holocene and Last Glacial Maximum (LGM) from oxygen isotopic ratios ($\delta^{18}O$) of individual foraminifera retrieved from deep-sea sediments. Our results document coordinated adjustments of the tropical Pacific/ENSO system between two diametrically opposite states: an "amplified ENSO" state in the LGM associated with a reduced zonal temperature gradient, and a "damped ENSO" state in the Mid-Holocene with enhanced gradient. Orbital precession provided the switch between these states and acted as the dominant external driver of the tropical Pacific/ENSO system in the past 25,000 years. The linked response of the mean state and variability to orbital forcing provides an integrated framework for testing ENSO theory and models.

Citation: Koutavas, A., and S. Joanides (2012), El Niño–Southern Oscillation extrema in the Holocene and Last Glacial Maximum, *Paleoceanography*, *27*, PA4208, doi:10.1029/2012PA002378.

1.   Introduction

[2]   ENSO is the principal mode of interannual climate variability on Earth notable for both its large amplitude and global scope [*McPhaden et al.*, 2006]. Its origin lies in coupled ocean-atmosphere interactions in the tropical Pacific Ocean, which are inherently unstable and oscillate between warm (El Niño) and cold (La Niña) states with a period of 3–7 years [*Bjerknes*, 1969; *Wang and Fiedler*, 2006]. The instrumental record suggests ENSO is modulated at lower frequencies [*Fedorov and Philander*, 2001], but its length is too short to evaluate potential ENSO adjustments on decadal and longer time scales relevant for society. Stability analysis suggests ENSO is dependent on the mean climate [*Fedorov and Philander*, 2001] raising concern that future climate change may profoundly affect ENSO behavior

[*Collins et al.*, 2010] with widespread consequences. Despite the obvious significance of this problem, especially for densely populated tropical regions where agriculture, food security, and human health are vulnerable to weather anomalies, reliable long-range ENSO prediction remains beyond the capability of current generation climate models [*Cane*, 2005; *Guilyardi et al.*, 2009; *Collins et al.*, 2010].

[3]   ENSO reconstructions from paleoclimate archives can extend the instrumental record and provide valuable insights on long-term ENSO dynamics as well as targets for model investigations. Coral-based reconstructions from the tropical Pacific have been especially valuable for gaining direct insight into oceanic ENSO processes [*Tudhope et al.*, 2001; *McGregor and Gagan*, 2004; *Cobb et al.*, 2003] but are limited in spatial and temporal distribution resulting in short and discontinuous records. Coral specimens predating the Holocene (last 10,000 years) are exceedingly rare, and consequently ENSO understanding over glacial-interglacial cycles has been at an effective standstill [*Tudhope et al.*, 2001]. Constraints during the LGM ~19–24 ka (thousand years ago) in particular are virtually non-existent yet highly desirable as this period has long been a benchmark for paleoclimate reconstructions and modeling [*Otto-Bliesner et al.*, 2003; *Zheng et al.*, 2008].

[4]   In order to develop long and continuous ENSO reconstructions from the ocean environment we used an alternative approach based on planktonic foraminifera from seafloor sediments [*Koutavas et al.*, 2006; *Leduc et al.*, 2009]. Over their short life spans (order of one month or less) foraminifera construct shells of calcite ($CaCO_3$) capturing brief snapshots of sea surface temperature (SST) and salinity in their oxygen-

[1]Department of Engineering Science and Physics, College of Staten Island, City University of New York, Staten Island, New York, USA.
[2]Doctoral Program in Earth and Environmental Sciences, Graduate Center of the City University of New York, New York, New York, USA.
[3]Lamont-Doherty Earth Observatory, Columbia University, Palisades, New York, USA.
[4]Environmental Science Program, College of Staten Island, City University of New York, Staten Island, New York, USA.
[5]Now at Los Gatos Union School District, Los Gatos, California, USA.

Corresponding author: A. Koutavas, Department of Engineering Science and Physics, College of Staten Island, City University of New York, 2800 Victory Blvd., Staten Island, NY 10314, USA. (tom.koutavas@csi.cuny.edu)
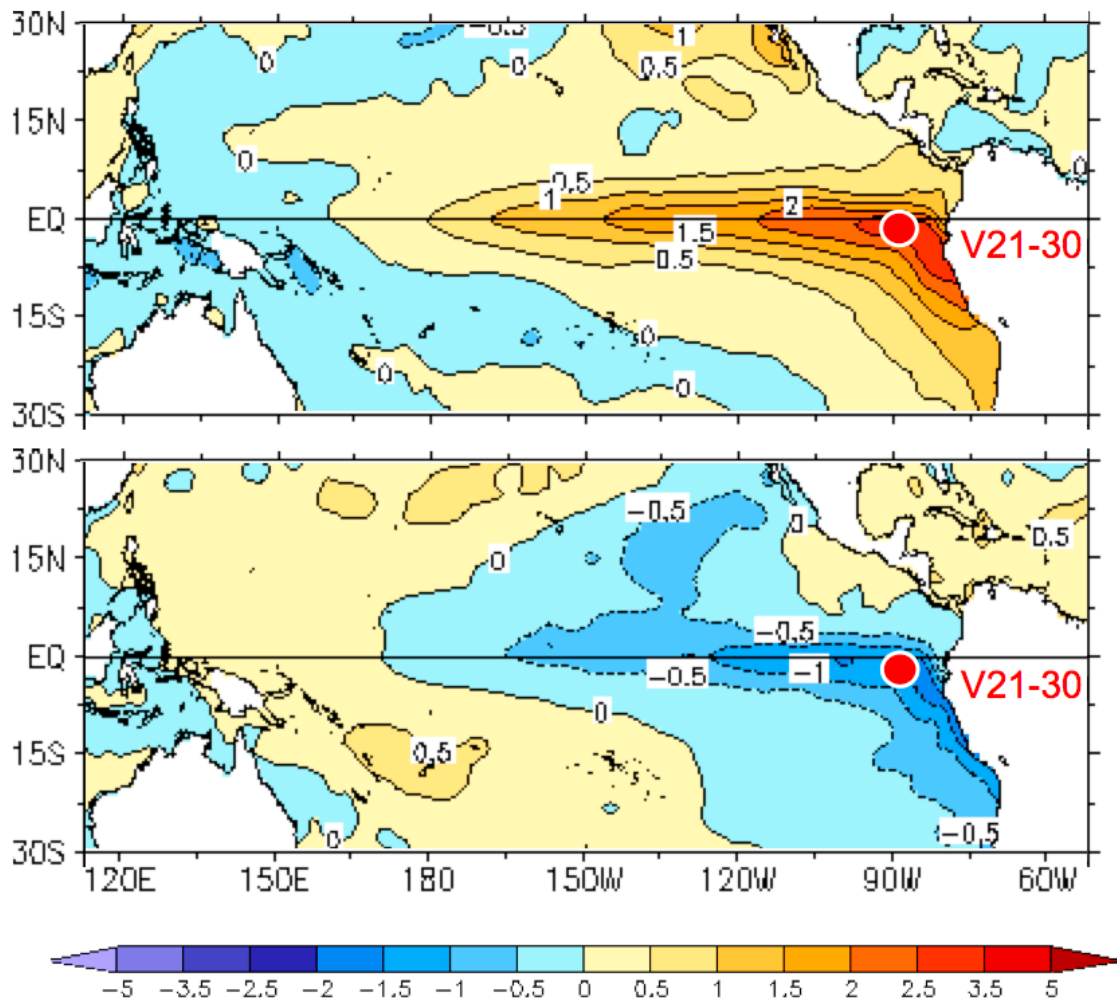
Figure 1. Location of core V21–30 with respect to annual SST anomalies (January through December) during the (top) 1997 El Niño and (bottom) 2007 La Niña (from Global Ocean Data Assimilation System, accessed at http://www.cpc.ncep.noaa.gov/products/GODAS/monthly.shtml).

isotopic ratio (δ^{18}O). Analysis of individual specimens deposited over narrow intervals allows an estimation of the corresponding monthly variability. We use *Globigerinoides ruber* (white), a surface-dwelling species prolific in the tropical oceans, which offers distinct advantages because of its mixed-layer habitat [*Fairbanks et al.*, 1982], short life span of 2–4 weeks [*Spero*, 1998], broad temperature and salinity tolerances [*Bijma et al.*, 1990], and high abundance in sediments of the tropical Pacific. Building on earlier results demonstrating this method's potential [*Koutavas et al.*, 2006] we present here a comprehensive data set of individual *G. ruber* δ^{18}O spanning the Holocene and LGM from sediment core V21–30 in the eastern equatorial Pacific (EEP) near the Galapagos Islands (Figure 1).

[5] The main controls on *G. ruber* δ^{18}O are the calcification temperature ($-0.21‰/°C$) [*Bemis et al.*, 1998] and salinity ($0.27‰/psu$) [*Fairbanks et al.*, 1982]. The seasonal range of SST and salinity at our site is 5.3°C and 1.4 psu respectively, increasing interannually to 10.8°C and 1.8 psu [*Carton and Giese*, 2008]. During El Niño warming and freshening drive δ^{18}O depletion, while during La Niña cooling and drying drive enrichment. SST dominates over

salinity accounting for 90% of the total δ^{18}O variance. Consequently interpretations of *G. ruber* δ^{18}O are framed here primarily in terms of SST (amplified by a synergistic salinity effect). Our method quantifies the integrated SST variance rather than interannual SST anomalies due to ENSO. Shifts in variance may therefore also result from changing seasonality, and accordingly we qualify our results with respect to this possibility. Decadal and longer variations are neglected because their longer periods (and likely smaller amplitude) strongly diminish their contribution to the measured δ^{18}O variance.

2. Material and Methods

[6] Core V21–30 (1°13′S, 89°41′W, 617 m depth) is located within the equatorial cold tongue of the EEP formed by divergent upwelling, and experiences large SST anomalies correlated strongly with the Niño-3 index ($r = 0.83$ for Nov 1981–Sep 2011) (Figure 1). For this project δ^{18}O was measured on 2071 *G. ruber* specimens from 39 Holocene and LGM samples, averaging 53 ± 7 individuals per sample. Based on mean sedimentation rate of ~13 cm/ka over the

Table 1. Carbon-14 Ages on *N. dutertrei* Used in the Age Model of V21–30[a]

Sample Depth (cm)	Raw C-14 Age (yr)	Age Error (±yr)	Calibrated Age (yr)	Lab	Accession Number	References
0	2190	45	1640	NOSAMS	OS-20675	*Koutavas and Lynch-Stieglitz* [2003]
55	5620	55	5880	NOSAMS	OS-30482	*Koutavas and Lynch-Stieglitz* [2003]
120	9830	55	10600	NOSAMS	OS-20674	*Koutavas and Lynch-Stieglitz* [2003]
151	11250	50	12740	NOSAMS	OS-20676	*Koutavas and Lynch-Stieglitz* [2003]
170	11750	90	13100	NOSAMS	OS-30483	*Koutavas and Lynch-Stieglitz* [2003]
184	12250	70	13570	NOSAMS	OS-30484	*Koutavas and Lynch-Stieglitz* [2003]
211	15750	40	18640	UCIAMS	46973	*Stott et al.* [2009]
215	13400	90	15250	NOSAMS	OS-30485	*Koutavas and Lynch-Stieglitz* [2003]
225	15650	70	18400	UCIAMS	47875	*Stott et al.* [2009]
225	16520	80	19190	UCIAMS	47876	*Stott et al.* [2009]
236	17550	80	20150	UCIAMS	47877	*Stott et al.* [2009]
236	17430	80	20060	UCIAMS	47878	*Stott et al.* [2009]
241	16710	90	19300	UCIAMS	47879	*Stott et al.* [2009]
241	17140	80	19740	UCIAMS	47880	*Stott et al.* [2009]
250	16800	80	19360	NOSAMS	OS-20680	*Koutavas and Lynch-Stieglitz* [2003]
300	22100	130	25940	NOSAMS	OS-46188	*Koutavas and Lynch-Stieglitz* [2003]
300	22800	90	26260	NOSAMS	OS-46262	*Koutavas and Lynch-Stieglitz* [2003]
320	25100	150	29390	NOSAMS	OS-30486	*Koutavas and Lynch-Stieglitz* [2003]
400	26900	150	31640	NOSAMS	OS-15720	*Koutavas and Lynch-Stieglitz* [2003]
520	36400	250	41150	NOSAMS	OS-20678	

[a]NOSAMS, National Ocean Sciences Accelerator Mass Spectrometer; UCIAMS, University of California Irvine Accelerator Mass Spectrometer.

past 25 ka and sampling width of 1 cm each sample represents a nominal deposition interval of ∼80 years, although the effective interval is likely longer due to bioturbation. The site lies near the modern oxygen minimum zone, with dissolved [O₂] of ∼1 ml/l, a factor that may provide a relative advantage by limiting benthic activity. Additional observations suggest that bioturbation is not a serious impediment to our method, notably because samples closest to the deglacial interval of the core, hence most susceptible to admixture of individuals with different isotopic composition, show no evidence of such admixture. A more detailed evaluation of bioturbation is given in the results section.

[7] The age model of core V21–30 is based on a linear regression of twenty C-14 ages (R² = 0.977) on *Neogloboquadrina dutertrei* between 0 and 520 cm depth [*Koutavas and Lynch-Stieglitz*, 2003; *Stott et al.*, 2009] listed in Table 1. This differs from a previous age model based on linear interpolation of a subset of these ages [*Koutavas et al.*, 2002; *Koutavas and Lynch-Stieglitz*, 2003]. The C-14 ages were calibrated here using CALIB 5.0.1 with ΔR of 125 years (the regional departure from the global average reservoir correction) and uncertainty of ±66 years [*Stuiver and Reimer*, 1993]. Ages beyond the CALIB range were calibrated according to *Fairbanks et al.* [2005]. Additional C-14 ages on this core are available from *G. ruber*, *G. sacculifer* and *G. menardii* [*Stott et al.*, 2009] all indicating linear accumulation rate, but species age offsets are also present. We chose *N. dutertrei* for the age model because of the greater number of ages available, higher species abundance allowing larger samples to be analyzed, and C-14 ages intermediate to the other species. We emphasize that the assumptions built into this age model (linear regression, choice of species, reservoir correction, etc.) contribute uncertainties that collectively can amount to several hundred years. The chronology of events and suggested sub-epoch boundaries delineated in our data (e.g., Late, Middle and Early Holocene) should therefore be considered approximate and elastic. Comparisons with other records from the tropical

Pacific dated either with C-14 or other clocks, for example U/Th in corals and speleothems, are also subject to this caveat.

[8] Paired Mg/Ca and $\delta^{18}O$ in V21–30 were measured on ∼100 pooled *G. ruber* from the 250–355 μm size-fraction. Samples were gently crushed, homogenized and split in 2–3 aliquots for replicate Mg/Ca and $\delta^{18}O$. Splits for Mg/Ca underwent clay removal and oxidative and reductive cleaning to remove authigenic oxides and sulfides, and were analyzed on a Jobin-Yvon Panorama-V ICP-OES at Lamont-Doherty Earth Observatory (LDEO). Analytical precision, expressed as the pooled standard deviation of 60 replicate pairs, was ±0.0464 mmol/mol, equivalent to ±0.2°C. Temperature was calculated with the equation Mg/Ca = 0.38*exp(0.09T) where Mg/Ca is in mmol/mol, and T in °C [*Dekens et al.*, 2002; *Anand et al.*, 2003]. Aliquots for stable isotopes from the same samples were measured on a VG Optima Isotope Ratio Mass Spectrometer (IRMS) following reaction with phosphoric acid at 90°C. $\delta^{18}O$ and $\delta^{13}C$ were calibrated to Vienna Pee-Dee Belemnite (VPDB) by repeat analyses on NBS-19 and an internal laboratory standard. Analytical precision was ±0.06‰ for $\delta^{18}O$ and ±0.04‰ for $\delta^{13}C$. Individual *G. ruber* were picked from the 300–355 μm size fraction, cleaned ultra-sonically in deionized water, and analyzed on a VG Optima IRMS at LDEO, and an identical instrument at Rutgers University. Both instruments were calibrated with NBS-19 and an identical internal working standard, and both had comparable precision of ±0.1‰ for $\delta^{18}O$. The isotopic composition of seawater ($\delta^{18}O_{sw}$) was calculated with the low-light equation of *Bemis et al.* [1998]: $T(°C) = 16.5(\pm 0.1) - 4.8(\pm 0.08)*(\delta^{18}O_c - \delta^{18}O_{sw})$, where T is the temperature from Mg/Ca, and $\delta^{18}O_c$ the isotopic composition of *G. ruber* calcite.

3. Core Stratigraphy and Comparison With Modern Conditions

[9] The full suite of measured proxies in core V21–30 is illustrated in Figure 2. These include bulk *G. ruber* $\delta^{18}O$ and
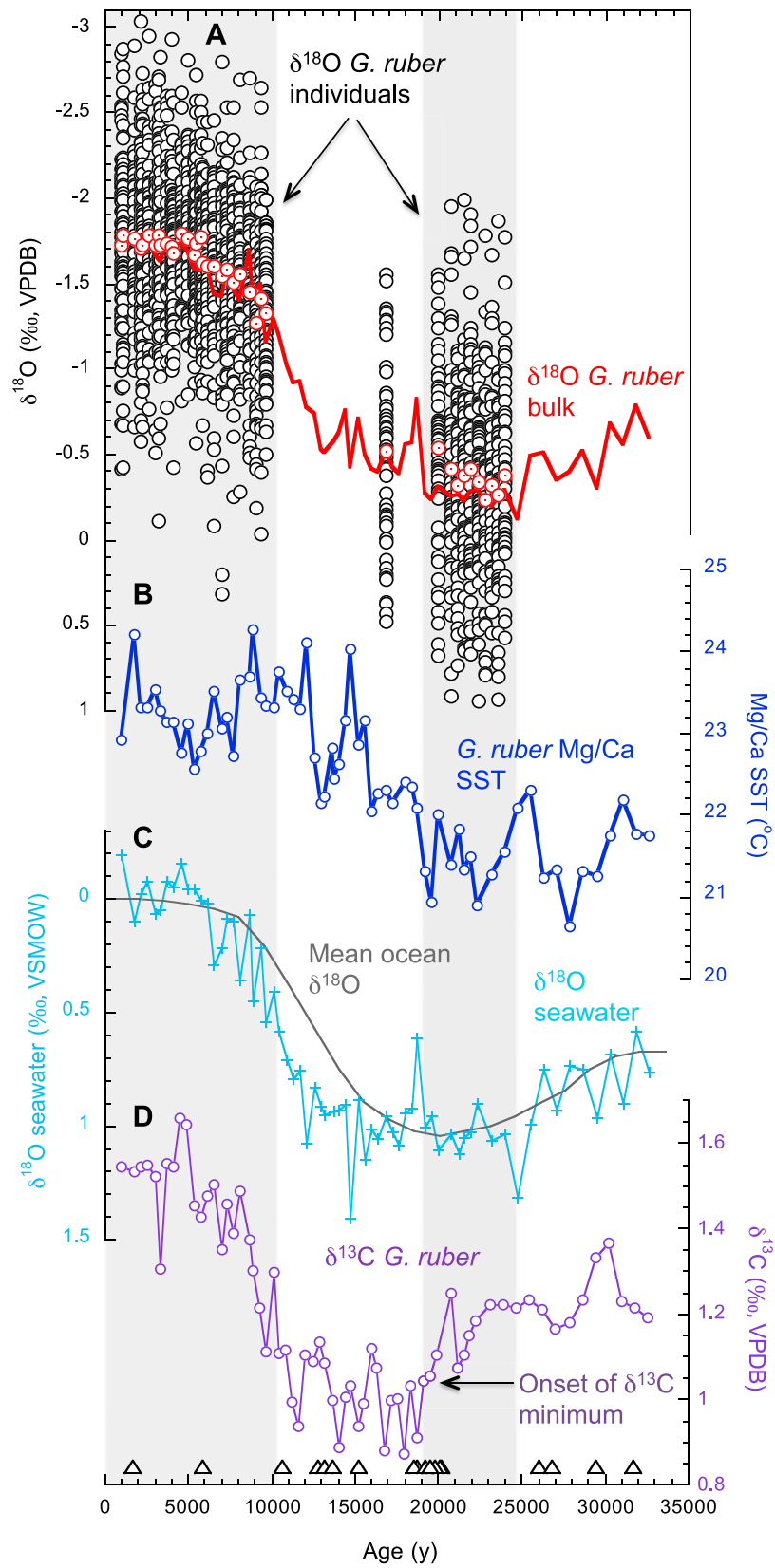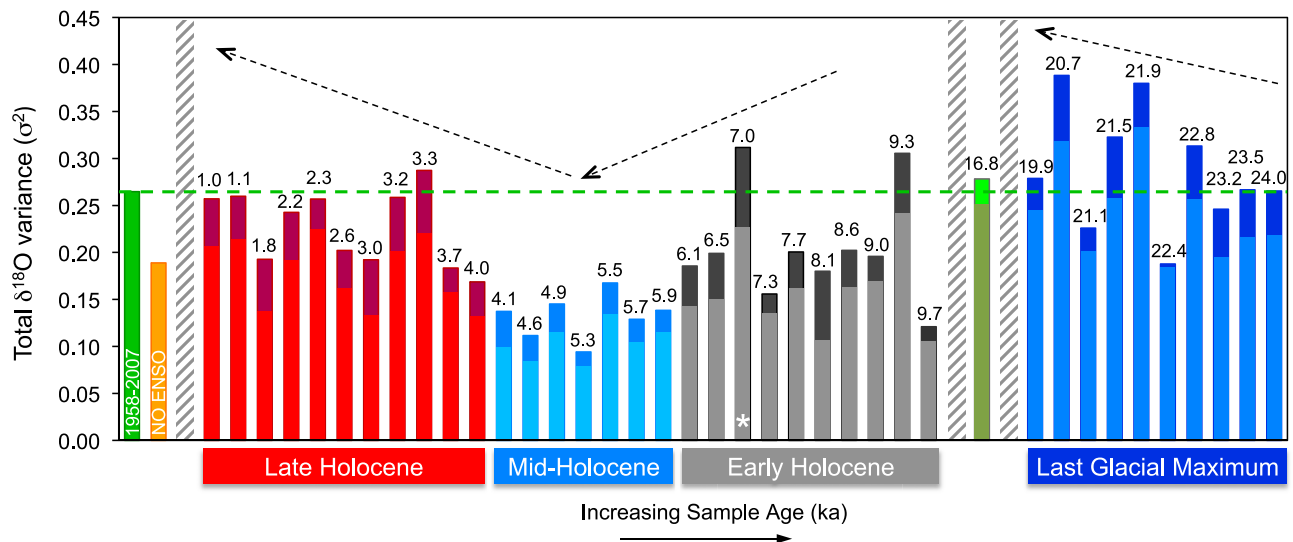
Figure 2

Figure 3. $\delta^{18}O$ variance of individual *G. ruber* from the Holocene and LGM. The variance is calculated as the squared standard deviation (σ^2) of individual $\delta^{18}O$ in each sample. Two bars are shown for each sample: the high bar includes all the data while the low bar excludes the heaviest and lightest value from each distribution, to test for spurious outlier effects. Both approaches yield similar shifts in variance downcore. The age of each sample is indicated at the top of each bar (rounded to 0.1 ka). The 1.1 ka sample is the core top of V21–29. The 7.0 ka sample marked with a star appears anomalous as its variance is driven by two positive outliers (>3-sigma from the mean) and may be spurious. This sample was excluded from further analysis. Green bar on left and dashed horizontal line indicate the 1958–2007 monthly $\delta^{18}O$ variance from instrumental SST and salinity [*Carton and Giese*, 2008]. Orange bar marked "No ENSO" is the monthly variance due to the annual cycle only [*Locarnini et al.*, 2006]. Dashed arrows suggest broad trends in the data. Hatched bars mark data breaks.

$\delta^{13}C$, Mg/Ca SST, $\delta^{18}O$ of seawater ($\delta^{18}O_{sw}$), $\delta^{18}O$ of individual *G. ruber* (N = 2071), and C-14 ages used in the age model (Table 1). Stratigraphic relationships are consistent with other open-ocean cores from the EEP [*Lea et al.*, 2006; *Pena et al.*, 2008] establishing the site as representative. The LGM is defined by maximum $\delta^{18}O$ enrichment (Figure 2a) terminating ~19 ka with a warming step in Mg/Ca SST (Figure 2b) and a correlative negative $\delta^{13}C$ shift (Figure 2d) previously observed in other sites from the EEP [*Spero and Lea*, 2002; *Pena et al.*, 2008]. The SST amplitude from LGM to Late Holocene averages 2.0°C (Figure 2b), similar to the ~1.8°C change in nearby core TR163–22 [*Lea et al.*, 2006]. V21–30 also shows a ~1.5°C deglacial reversal during the Younger Dryas, a previously ambiguous signal in Mg/Ca but more clear in alkenone records [*Kienast et al.*, 2006]. The $\delta^{18}O_{sw}$ calculated from *G. ruber* $\delta^{18}O$ and Mg/Ca shows a mean LGM-Holocene shift of 1‰ consistent with the mean ocean shift due to ice volume [*Waelbroeck et al.*, 2002] but with a lag during deglaciation evident also in nearby TR163–22 [*Lea et al.*, 2006]. A key advantage of V21–30 is its shallow depth, which minimizes carbonate dissolution and contributes to superior preservation and high abundance of *G. ruber*. Our main objective here is to exploit these attributes for single-specimen $\delta^{18}O$ analysis to reconstruct shifts in variance.

[10] The full ensemble of individual *G. ruber* $\delta^{18}O$ is shown in Figure 2a, and the corresponding estimates of variance are shown in Figure 3. As a test of our method's ability to reproduce modern conditions we compared the mean and variance of $\delta^{18}O$ in core top samples with expected values from instrumental data. Two core tops with ages of 0.96 and 1.06 ka from V21–30 (617 m water depth) and nearby V21–29 (712 m water depth) [*Koutavas and Lynch-Stieglitz*, 2003] produced identical $\delta^{18}O$ distributions with means of −1.72 and −1.78‰ and standard deviations of 0.507 and 0.510‰. By comparison expected values from instrumental (1958–2007) monthly SST and salinity [*Carton and Giese*, 2008] average −1.55 to −1.88‰ (bracketed by the equations of *Bemis et al.* [1998]) and standard deviation of 0.514‰. The core top and late twentieth century values are indistinguishable indicating the method faithfully captures both mean and variance. We proceed to examine reconstructed monthly variance in the past from *G. ruber* $\delta^{18}O$.

4. Holocene

[11] The complete sequence of reconstructed $\delta^{18}O$ variance (σ^2) in our samples is shown in Figure 3. For reference the figure also shows the late twentieth century variance calculated from instrumental data [*Carton and Giese*, 2008] (green

Figure 2. Stratigraphic and paleoclimatic proxies from core V21–30. (a) $\delta^{18}O$ of bulk *G. ruber* (red line), $\delta^{18}O$ of *G. ruber* individuals (open circles) and their mean values (red circles). (b) Mg/Ca SST of *G. ruber*. (c) $\delta^{18}O$ of seawater calculated from *G. ruber* Mg/Ca and $\delta^{18}O$, compared to global ocean $\delta^{18}O$ [*Waelbroeck et al.*, 2002]. (d) $\delta^{13}C$ of *G. ruber*. Triangles at bottom indicate C-14 ages used in the age model (Table 1). The Holocene and LGM are shaded in gray.

bar on left), and the expected variance in a hypothetical scenario without ENSO but with unchanged seasonal cycle (orange bar). Removal of ENSO reduces the variance by 29% from 0.265 to 0.189, highlighting the dominance of annual over interannual variability in the EEP today [*Wang and Fiedler*, 2006]. Six of nine samples (66%) within the last 3.5 ka yield indistinguishable variance from the twentieth century while three others are somewhat reduced. As a whole the Late Holocene (0–4 ka) has average variance of 0.224, 15% less than the twentieth century, with some evidence of millennial variability. Although not robust at current resolution, the latter merits further investigation. Prior to ∼3.5 ka, Holocene variance was distinctly lower, with only 2 of 19 samples (10%) reaching twentieth century values. Most distinct is a ∼2,000-year period between ∼4–6 ka marked by a deep minimum (Figure 3). We use the term "Mid-Holocene" to describe this interval, but caution that other studies may define the Mid-Holocene somewhat differently. For example the Paleoclimate Modeling Intercomparison Project (PMIP) applies the term "Mid-Holocene" to 6 ka [*Zheng et al.*, 2008], and other studies may consider the Mid-Holocene to extend earlier to ∼7 ka. We calculated the mean variance of the 4–6 ka interval to be 0.134 or ∼50% less than modern. This reduction agrees qualitatively with previous inferences of Mid-Holocene ENSO decline from western Pacific corals [*Tudhope et al.*, 2001; *McGregor and Gagan*, 2004] although the minimum variance in our data is somewhat later that the coral ages in those studies (∼6.5 ka and 5.35–6.09 ka, respectively). Reduced Mid-Holocene ENSO is also supported by sediments from lakes Pallcacocha in Ecuador [*Moy et al.*, 2002] and El Junco in the Galapagos [*Conroy et al.*, 2008], although there are also notable differences between our results and these lake records, discussed below.

[12] An alternative attribution of the reduced Mid-Holocene variance in our samples might be due to a damped annual cycle. We do not favor this as the primary driver because it fails to explain corroborating evidence for damped ENSO, including from western Pacific corals [*Tudhope et al.*, 2001; *McGregor and Gagan*, 2004] where seasonality is extremely small. However, the magnitude of our Mid-Holocene anomaly is too large to explain by ENSO decline alone (Figure 3) and calls for an additional source, most likely from a weaker annual cycle. A damped annual cycle may have resulted from a northward shift of the Intertropical Convergence Zone (ITCZ) [*Haug et al.*, 2001] to latitudes farther removed from the equator allowing steadier year-round upwelling. This is consistent with Mid-Holocene cooling of ∼0.5°C observed at our core site (Figure 2b) and similar cooling off Baja California [*Marchitto et al.*, 2010] - a region teleconnected to the EEP today - implying a regionally coherent SST anomaly. Eastern Pacific cooling and a stronger zonal gradient at this time [*Koutavas et al.*, 2006; *Marchitto et al.*, 2010] evoke sustained La Niña conditions, an analogy that resonates with enhanced aridity in the Great Basin and Rocky Mountains of the western United States [*Benson et al.*, 2002; *Bacon et al.*, 2006; *Shuman et al.*, 2009], regions that experience drought today during La Niña (or lack of El Niño). For example, Owens Lake in California reached near-desiccation levels ∼4.3–6.8 ka [*Bacon et al.*, 2006], while Rocky Mountain lakes

experienced low stands ∼4.5–7.0 ka [*Shuman et al.*, 2009] largely overlapping the period of damped variance and cooling in our EEP reconstruction. Our attribution of the anomalous Mid-Holocene variance to a combination of suppressed ENSO and weaker seasonality is also consistent with the majority of models surveyed by a recent ∼6 ka PMIP-2 synthesis [*Zheng et al.*, 2008]. Four out of seven models indicated reduced seasonal amplitude in the Niño-3 region with the remaining three indicating no change, while six of the seven models also simulated weakened ENSO amplitude.

[13] The Early Holocene (6.0–9.7 ka) has mean variance of 0.199, which is intermediate between the Late and Mid-Holocene (Figure 3). Compared to the core top values this represents a significant decrease of 23%, but it is unclear what portion of this reflects reduced ENSO versus damped seasonality. Interannual events are discernible in corals during this timeframe but with damped amplitude [*McGregor and Gagan*, 2004], suggesting ENSO was weaker but operating. Our results are in agreement with this notion and suggest the Early Holocene was a dynamically similar but probably less extreme precursor of the Mid-Holocene. This view is also consistent with the lake record from El Junco [*Conroy et al.*, 2008] where the greatest ENSO decline appears to have occurred between 4 and 6 ka, but contrasts with Pallcacocha [*Moy et al.*, 2002] where ENSO was found to be least active in the early Holocene (see Figures 7b and 7c for a comparison of these lake records with our results). Considering that the lake records may be biased toward moderate-to-strong positive (El Niño) events only, and that our results do not explicitly separate seasonality effects from ENSO, we should not be surprised by these differences. While further refinements are needed, the first-order agreement of these records on a long-term increase in ENSO through the Holocene is reassuring.

[14] Our earliest Holocene sample dates to 9.7 ka and is stratigraphically located directly above the large deglacial $\delta^{18}O$ shift (Figure 2a). As such this sample is most vulnerable to admixture of isotopically heavier individuals from underlying stratigraphic levels due to bioturbation. Such individuals would be identifiable by their significantly heavier isotopic values, resulting in a skewed distribution and artificially enhanced $\delta^{18}O$ variance. However, none of these characteristics are present. The 9.7 ka sample has one of the lowest variances in the entire Holocene (Figure 3), no evident skewness, and no suspect outlier values indicating upward transport from lower stratigraphic levels. These observations increase our confidence that bioturbation is not an insurmountable impediment to our approach.

5. LGM

[15] Direct constraints of LGM ENSO from the tropical Pacific have heretofore been elusive. Our $\delta^{18}O$ index registers maximum variance during this time (Figure 3) with a mean of 0.284, 27% greater than the Late Holocene mean (0–4 ka) and 7% greater than late twentieth century. Four out of ten LGM samples significantly exceed the twentieth century variance by up to 46%. Compared with the Middle and Early Holocene, the LGM has 115% and 43% greater variance respectively. The highest LGM variance at 20.7 ka
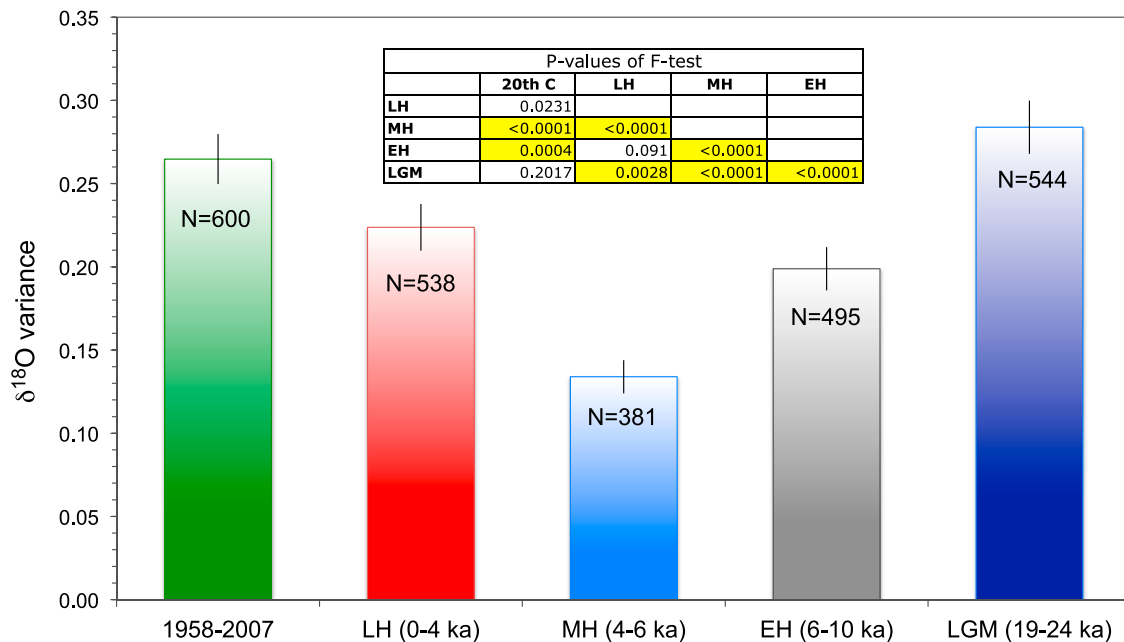
Figure 4. Variance of δ^{18}O of individual *G. ruber* pooled over the Late Holocene (LH), Mid-Holocene (MH), Early Holocene (EH) and Last Glacial Maximum (LGM), compared to the late twentieth century. The twentieth century variance (Jan 1958 to Dec 2007) was calculated from the monthly CARTON-GIESE SODA data [*Carton and Giese*, 2008] for the grid box containing the core site (89.75°W, 1.25°S). The error bars indicate the standard error of the variance: $\sigma^2 \sqrt{(2/(N-1))}$, where σ is the standard deviation and N the number of observations. P-values of *F* tests for equality of variance are indicated in the inset. P-values <0.01 are highlighted in yellow.

exceeds the lowest Mid-Holocene value at 5.3 ka by four-fold. *F* tests for equality of variance show that the differences between the Early, Middle, Late Holocene and LGM sample pools are significant at >99% confidence (Figure 4) (except Early versus Late Holocene, significant at 90%). As a whole these results attest to a remarkably large dynamic range in EEP conditions within the past 25 ka.

[16] Was the amplified LGM variance the outcome of stronger ENSO or enhanced seasonality? For an independent assessment of seasonality we turned to the meridional SST gradient between the cold tongue and the northeastern Pacific warm pool near 8°N (Figure 5). This gradient undergoes a pronounced seasonal variation coupled to the cold-tongue/ITCZ complex and its strength has been shown in models to be intimately linked to the annual cycle variance [*Timmermann et al.*, 2007]. Assessment of this gradient therefore provides an indirect means to constrain seasonality. A significant reduction of this gradient was previously proposed for the LGM on the basis of planktonic δ^{18}O records within the EEP [*Koutavas and Lynch-Stieglitz*, 2003]. Later studies using alkenone paleothermometry suggested the opposite pattern, i.e., an intensified LGM gradient [*Dubois et al.*, 2009; *Rincón-Martínez et al.*, 2010]. However, alkenone reconstructions in warm ocean regions are subject to some ambiguity due to decreasing response of the alkenone unsaturation index with increasing temperature above 26°C [e.g., *Conte et al.*, 2006]. Studies that account for this effect give significantly different results from those that do not, even within the same core (see, for example,

Leduc et al. [2007] versus *Dubois et al.* [2009] and *Rincón-Martínez et al.* [2010] for core MD02–2529). Caution is therefore needed when interpreting alkenone results from the warm province north of the cold tongue where SSTs reach >28°C. Given these considerations we turned again to δ^{18}O and undertook an updated synthesis of *G. ruber* δ^{18}O records to reevaluate the EEP gradient (Table 2). The results (Figure 5) indicate a reduced LGM gradient by 35%, which we interpret as the combined effect of reduced SST and salinity gradients across the equatorial front. On this basis we infer that the seasonal cycle of the cold tongue was likely weaker during the LGM and hence not the source of the amplified δ^{18}O variance, pointing instead to ENSO as the most plausible driver. Dynamically, reduced LGM seasonality could be explained by means of restricted northward migration of the ITCZ in boreal summer, forced by high-latitude ice cover [*Chiang and Bitz*, 2005]. This would have resulted in a net southward shift of the mean ITCZ position and a narrower seasonal migration range, with reduced seasonality of SST (due to less variable winds seasonally) and precipitation in the equatorial cold tongue. A southward-shifted ITCZ implies greater mean annual rainfall, other factors being equal. This is not supported by the δ^{18}O$_{sw}$ record (Figure 2c), which does not show a negative excursion during the LGM. We interpret this to reflect a compensating decrease in rainfall due to cooler SSTs and weakened atmospheric convection. *Rincón-Martínez et al.* [2010] also found decreased rainfall in Ecuador based on diminished terrigenous inputs to a coastal marine site from
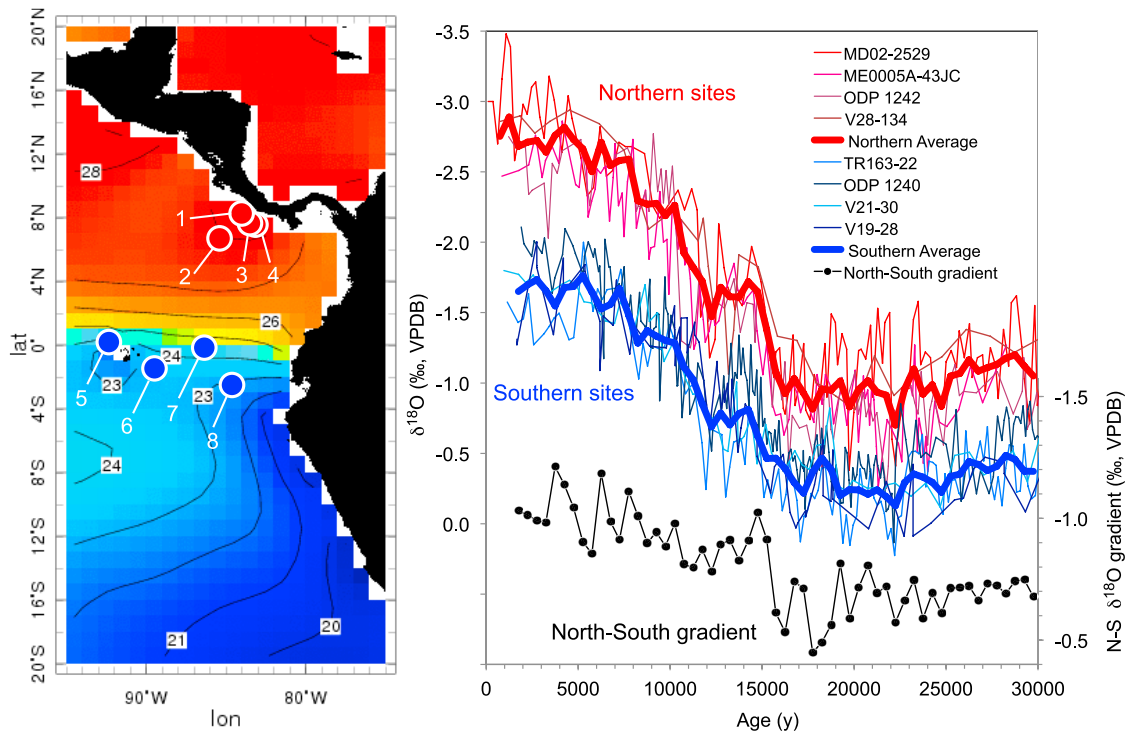
Figure 5. Meridional gradient of the eastern tropical Pacific from *G. ruber* δ^{18}O. (left) The map illustrates the modern gradient in annual mean SST from World Ocean Atlas 2005 data [*Locarnini et al.*, 2006], and the locations of eight cores with *G. ruber* δ^{18}O data, used to reconstruct the gradient over the last 30 ka. Cores are numbered as in Table 2. (right) *G. ruber* δ^{18}O profiles from these cores. Averages of the four northern and four southern sites are shown in thick red and blue lines, calculated by averaging the raw data in 500-year windows. The N-S δ^{18}O gradient (black circles at bottom right) is calculated as the difference between the northern and southern averages. The mean LGM gradient (0.68‰) reflects a 35% reduction relative to the Late Holocene (1.05‰).

nearby rivers. While those authors attributed the more arid glacial stages in Ecuador to a northward shift of the ITCZ, this interpretation remains difficult to reconcile with our finding of a relaxed δ^{18}O gradient between 8°N and 2°S (Figure 5). Alternatively, arid glacials in Ecuador may reflect a general weakening of the hydrologic cycle or a decoupling of terrestrial and marine rainfall responses.

[17] As with the Holocene, the LGM sample most susceptible to bioturbation artifacts is the one stratigraphically closest to the deglaciation (19.9 ka). This sample shows no evidence of isotopically light outliers originating in the overlying deglacial interval, nor unusually high variance or negative skewness as might be expected from admixture of younger individuals with more negative δ^{18}O. To further evaluate the role of bioturbation we analyzed one sample from the deglacial interval (16.8 ka), hypothesizing that it would be most likely to display anomalously high variance from admixture of both heavier and lighter outliers from above and below. Once again we found no isotopic outliers, or evidence of unusually high variance as a consequence of bioturbation. While these observations do not rule out

Table 2. *G. ruber* δ^{18}O Records From the Eastern Equatorial Pacific Used to Calculate the Meridional δ^{18}O Gradient of Figure 5[a]

	Core ID	Latitude	Longitude	Depth (m)	References
1	MD02–2529	8°12.33′N	84°07.32′W	1619	*Leduc et al.* [2007]
2	V28–134	6°54′N	85°25.98′W	2434	This study
3	ME0005A-43JC	7°51.35′N	83°36.5′W	1368	*Benway et al.* [2006]
4	ODP1242	7°51.35′N	83°36.42′W	1364	*Benway et al.* [2006]
5	TR163–22	0°30.9′N	92°23.9′W	2830	*Lea et al.* [2006]
6	V21–30	1°13′S	89°41′W	617	This study
7	ODP1240	0°01.31′N	86°27.76′W	2921	*Pena et al.* [2008]
8	V19–28	2°22′S	84°39′W	2720	This study

[a]Core numbers on left correspond to those on the map of Figure 5. Adding to previously published data we provide here new data from V28–134, V21–30 and V19–28.

bioturbation, as a whole they suggest it is not a serious limitation of our data and interpretations.

[18] Our LGM data offer the first direct assessment of ENSO variability from the marine environment of the EEP, and as such are not amenable to direct comparison with other studies. One exception is the related study of *Leduc et al.* [2009], which evaluated thermocline variability in the Costa Rica Dome from isotopic distributions of individual *N. dutertrei*, a thermocline dweller. That study found marginally reduced variability in the LGM, although the results were not statistically significant and were based on much smaller sample sizes than our work. Less direct inferences have also been drawn from varved sediments of Lake Challa in East Africa, where present-day rainfall is teleconnected to the tropical Pacific [*Wolff et al.*, 2011]. Reduced interannual variability in those records was linked to possibly weaker ENSO; however, it is also possible that atmospheric teleconnections between the tropical Pacific and East Africa were different in the LGM, confounding the interpretation of lake hydrology in terms of ENSO forcing.

[19] Unlike the Mid-Holocene, model results for ENSO and seasonality during the LGM are mixed, making comparisons with our interpretations more tenuous. In the PMIP-2 model synthesis of *Zheng et al.* [2008] a survey of four LGM simulations found one with a significant decrease in ENSO (CCSM3), one with a significant increase (MIROC3.2), and two with no significant change. No consensus emerged on seasonality either, with one model indicating an increase and three indicating no change or small decreases. Within the realm of those surveyed models MIROC3.2 appears to be qualitatively the most consistent with our LGM findings of amplified ENSO and decreased seasonality.

6. Relationship With the Mean State

[20] The mean state of the tropical Pacific is thought to be fundamental for the character of interannual variability [*Fedorov and Philander*, 2001; *Cane*, 2005; *Guilyardi et al.*, 2009; *Collins et al.*, 2010]. The zonal SST asymmetry between the cool east and warm west Pacific is an essential indicator of the ocean-atmosphere coupling at the heart of ENSO [*Bjerknes*, 1969]. A strong zonal gradient is associated with cool SST and a shallow thermocline in the east, enhancing the ocean-atmosphere coupling and allowing the winds to generate large SST anomalies, in turn feeding back on the winds. A weak gradient implies a deeper thermocline and weaker air-sea coupling. It is unclear whether either of these states is inherently associated with more or less active ENSO.

[21] In light of the significant shifts in variance within our results, we investigate whether a link exists between reconstructed variance and the zonal SST gradient. We estimated this gradient for the last ~30 ka using *G. ruber* Mg/Ca records from the western and eastern Pacific (Figure 6). Specifically we used seven published Mg/Ca reconstructions from the western Pacific within the 28°C isotherm, and two from the eastern Pacific cold tongue (Table 3). While SST may also be geochemically estimated from algal-derived alkenones [*Kienast et al.*, 2006; *Leduc et al.*, 2007; *Koutavas*

and Sachs, 2008; *Dubois et al.*, 2009; *Rincón-Martínez et al.*, 2010] these compounds are generally in low abundance and often below detection in sediments of the warm western Pacific, limiting their usefulness in estimating basin-wide gradients. In addition, warm-temperature calibration uncertainties complicate alkenone interpretations in the warm pool. The Mg/Ca approach shows a reduction of ~1°C in the zonal gradient during the last glacial period between 17 and 25 ka, and a ~0.5°C increase in the Early-Middle Holocene between 4 and 8 ka (Figures 6b and 7d). These periods broadly coincide with the extrema in $\delta^{18}O$ variance described earlier (Figures 3 and 7c). Indeed, linear regression of the $\delta^{18}O$ variance and zonal SST gradient (Figure 8b) shows a significant negative correlation ($r = -0.67$) associating greater variance with reduced gradient and vice versa. Within this parameter space the LGM and Mid-Holocene represent fundamentally opposite circulation states. The former was characterized by weak gradient and amplified variability, and the latter by strong gradient and reduced variability. Importantly, inverse relationships between ENSO variability and the zonal gradient have recently been found in long integrations of coupled climate models [*Karnauskas et al.*, 2012], suggesting they may represent an intrinsic property of low-frequency adjustment of the tropical Pacific. In our results both extremes (Mid-Holocene and LGM) were marked by cooler SSTs in the EEP (Figure 2b), although for different dynamical reasons. The LGM cooling was in our view a consequence of global forcings from greenhouse gases and albedo, while the Mid-Holocene represents dynamical ocean-atmosphere adjustment promoting greater equatorial divergence.

[22] An integral aspect of ENSO involves zonal displacement of the heavy precipitation over the western Pacific, eastward during El Niño, causing drought over Indonesia. Consequently we expect any skillful reconstruction of ENSO to be coherent with records of Indonesian rainfall. As a test, we compared our reconstructed EEP variance with the $\delta^{18}O$ of speleothems recording convective rainfall over Borneo [*Partin et al.*, 2007] (Figure 7a). A significant positive correlation exists between Borneo speleothem $\delta^{18}O$ and EEP variance ($r = 0.62$, Figure 8c), which is consistent with the modern relationship between El Niño and Indonesian drought. The coherence of the two data sets is particularly compelling during the Mid-Holocene (4–6 ka) when the most depleted $\delta^{18}O$ (highest precipitation) in Borneo coincided with minimum EEP variance (Figures 7a and 7c). Given that excess precipitation in the western Pacific is an established consequence of La Niña, this result bolsters our earlier analogy with sustained La Niña conditions for the Mid-Holocene mean state. Diminished Borneo rainfall in the LGM is also consistent with our finding of amplified ENSO, although additional factors due to tropical cooling must have contributed to this. Overall, the relationship between Borneo precipitation and EEP variance from *G. ruber* $\delta^{18}O$ (Figure 8c) reinforces our view that the latter is primarily an index of the low-frequency modulation of ENSO. Were this index instead driven primarily by annual cycle changes, we would expect a positive correlation with the meridional EEP gradient (Figures 5 and 7e) [*Timmermann et al.*, 2007]. Instead a weak negative correlation is present (Figure 8d).
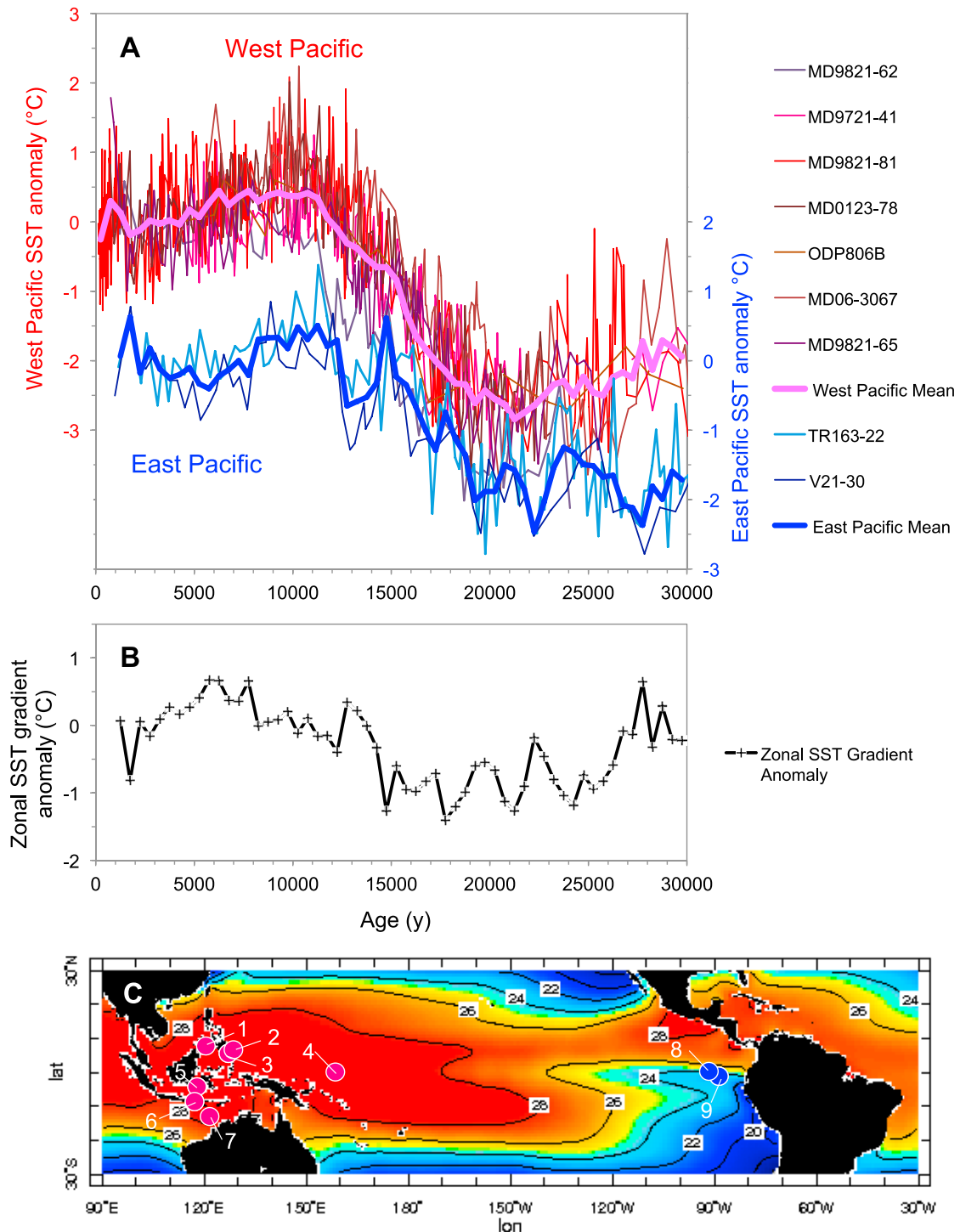
Figure 6. Zonal SST gradient of the tropical Pacific from *G. ruber* Mg/Ca. (a) Mg/Ca SST from seven western and two eastern Pacific cores (see also Table 3 for list of cores). SST is expressed as anomaly relative to the Late Holocene (0–4 ka) except for site MD9721–41 which lacks the Late Holocene and was instead referenced to 4–6 ka. The western Pacific records are plotted on the left axis and the eastern records on the right axis. The thick purple and blue lines represent the average for the western and eastern Pacific respectively, calculated by averaging the raw data in 500-year windows. (b) Zonal SST gradient anomaly relative to the Late Holocene calculated as the difference of the western and eastern Pacific averages from Figure 6a. (c) Locations of the nine cores relative to annual mean SST from World Ocean Atlas 2005 data [*Locarnini et al.*, 2006]. The core numbers follow Table 3. The western Pacific cores lie within the 28°C isotherm delineating the Indo-Pacific Warm Pool. The eastern Pacific cores lie within the equatorial cold tongue.

Table 3. *G. ruber* Mg/Ca SST Records Used to Calculate the East-West SST Gradient[a]

	Core ID	Latitude	Longitude	Depth (m)	References
1	MD9721–41	8°48′N	121°18′E	3633	*Rosenthal et al.* [2003]
2	MD06–3067	6°31′N	126°30′E	1575	*Bolliet et al.* [2011]
3	MD9821–81	6°18′N	125°49.8′E	2114	*Stott et al.* [2002]
4	ODP806B	0°19.1′N	159°21′E	2520	*Lea et al.* [2000]
5	MD9821–62	4°41.33′S	117°54.17′E	1855	*Visser et al.* [2003]
6	MD9821–65	9°39′S	118°20′E	2100	*Levi et al.* [2007]
7	MD0123–78	13°5′S	121°47′E	1783	*Xu et al.* [2008]
8	TR163–22	0°30.9′N	92°23.9′W	2830	*Lea et al.* [2006]
9	V21–30	1°13′S	89°41′W	617	This study
	ODP1240[b]	0°01.31′N	86°27.76′W	2921	*Pena et al.* [2008]

[a]The core numbers on left match those on the map of Figure 3.
[b]Site ODP1240 was not included in the east Pacific average because of concerns over dissolution affecting the Holocene SSTs. The combination of greater depth and a more westerly location (hence greater productivity) at this site pose an elevated risk of dissolution, particularly in the Holocene, the interval most prone to dissolution. Including this record in the east Pacific average however does not change the finding of weaker LGM zonal gradient.

[23] In summarizing the mean state constraints, both the zonal and meridional gradients of the tropical Pacific were weaker in the LGM (Figures 7d and 7e) and strengthened in the Holocene. The two gradients were estimated with different proxies (Mg/Ca and $\delta^{18}O$) and different sets of cores (Figures 5 and 6 and Tables 2 and 3) and are thus independent. Their convergence on a glacial mean state with diminished gradients supports earlier conceptual analogies with El Niño [*Koutavas et al.*, 2002; *Stott et al.*, 2002; *Koutavas and Lynch-Stieglitz*, 2003]. It remains unclear whether the LGM adjustment also involved changes in thermocline structure, an important element of the mean state [*DiNezio et al.*, 2011]. Thermocline reconstructions for the LGM are not fully developed, but some evidence based on isotopic gradients of vertically stratified foraminifera implies a thicker mixed layer and deeper thermocline in the eastern Pacific [*Spero et al.*, 2003]. Further work is necessary to constrain the LGM thermocline structure across the basin.

7. Causal Attribution

[24] The $\delta^{18}O$ variance correlates strongly ($r = 0.70$) with March–September insolation difference on the equator following the 23 ka precession cycle (Figures 7c and 8a). This relationship associates damped variance with maximum September (upwelling season) and minimum March (warm season) insolation, e.g., during the Mid-Holocene. Under this orbital configuration, reduced heating in March when the tropical Pacific is uniformly warm in east and west reduces heat input to the ocean and promotes cooling. In the opposite season (September) when equatorial upwelling intensifies, increased solar radiation restores heat in the west but not in the east Pacific where warming is opposed by dynamical upwelling; as a consequence the zonal gradient intensifies. This mechanism, known as the dynamical ocean thermostat [*Clement et al.*, 1996], reinforces the Walker circulation and opposes the development of El Niño [*Clement et al.*, 2000]. During the Early and Mid-Holocene this mechanism explains three key observations in our data: (i) cooling of the EEP (Figure 2b); (ii) enhanced zonal SST gradient (Figure 7d); and (iii) reduction of interannual variability (Figure 7c). During the LGM insolation was approaching the opposite orbital configuration (peaking ~17 ka, Figure 7c) with a corresponding prediction of weaker zonal gradient, enhanced ENSO, and warmer EEP. The first two are manifested in our data (Figures 7c and 7d) but the third was clearly overwhelmed by the global radiative forcings responsible for ice-age cooling. We conclude that despite the momentous shifts in background climate in the past 25 ka, precession remained the main control on zonal dynamics and interannual variability in the tropical Pacific, explaining 50% of the modulation of variance in *G. ruber* $\delta^{18}O$. This result suggests that orbital-scale ENSO variability may be largely predictable on the basis of insolation alone, a hypothesis that must be tested with longer records. However, the character of variability also includes abrupt regime shifts and higher-frequency volatility (e.g., the sharp transitions into and out of the Mid-Holocene and repeated oscillations during the LGM) that point to nonlinear behavior.

[25] Among our findings, the presence of amplified LGM ENSO is perhaps most unexpected, yet not entirely surprising. Some model simulations of the LGM climate produce enhanced ENSO activity [*Otto-Bliesner et al.*, 2003; *An et al.*, 2004; *Zheng et al.*, 2008], although for varying reasons and with background climate states not fully consistent with the one described here, i.e., one with reduced thermal gradients. The divergence of models on LGM ENSO [*Zheng et al.*, 2008; *DiNezio et al.*, 2011] resonates with a general lack of consensus on 21st century ENSO predictions [*Cane*, 2005; *Guilyardi et al.*, 2009; *Collins et al.*, 2010], highlighting the need for continued model development, testing and validation. Climate models are essential for anticipating ENSO surprises in a warming world and their skill hinges critically on faithfully reproducing paleo-ENSO reconstructions. Our evidence of diametrically opposite ENSO states in the Mid-Holocene and LGM coupled with coordinated adjustments of the mean state provides an integrated framework for validation experiments addressing both mean state and variability. Given the volatile nature of ENSO in the past 25 ka evident in our data, understanding its role in past and future climates should be a priority.
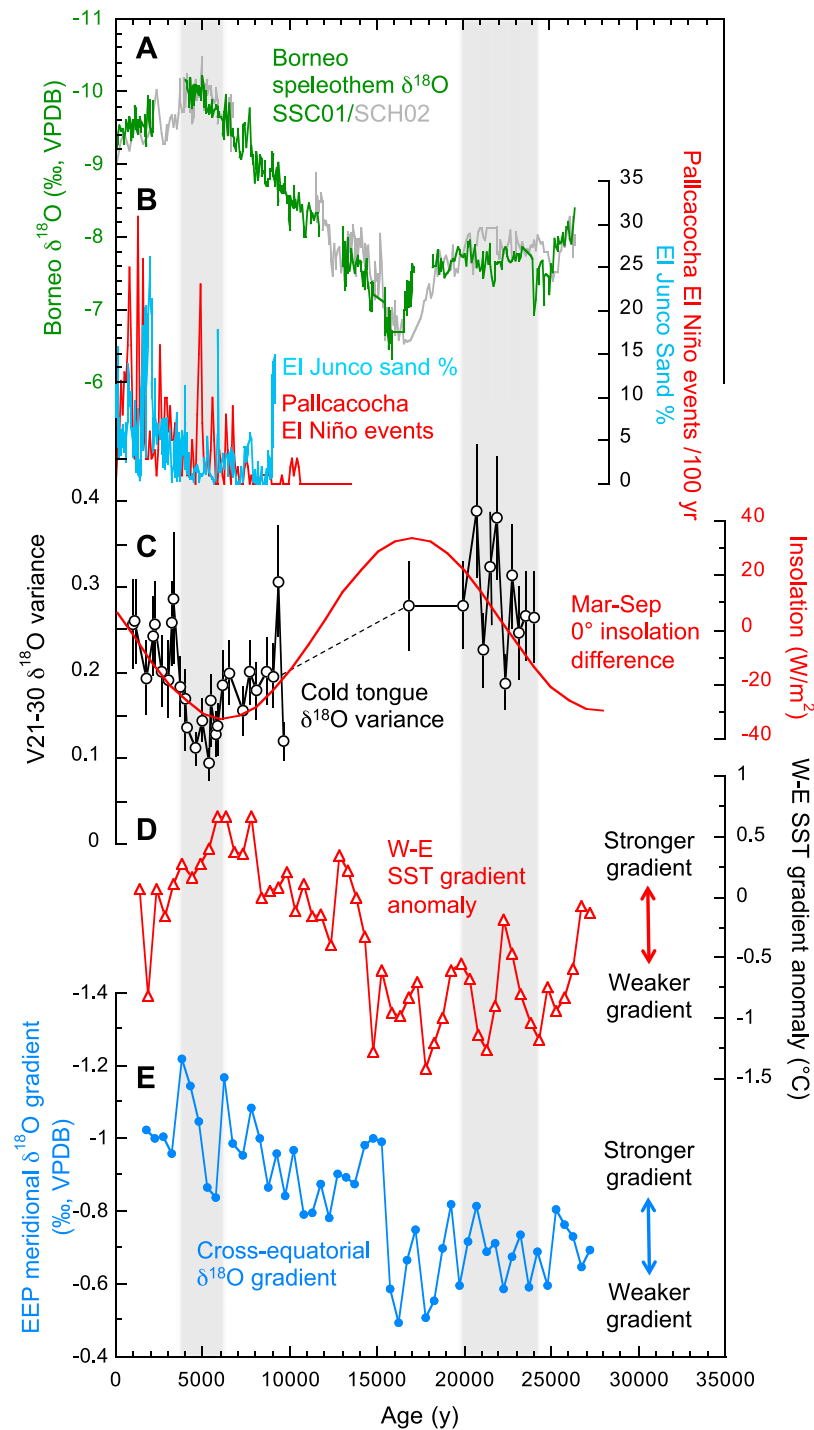
Figure 7. Synthesis of tropical Pacific climate proxies for the last 25 ka. (a) Borneo stalagmite δ^{18}O [*Partin et al.*, 2007]. (b) El Niño variability from lakes Pallcacocha, Ecuador [*Moy et al.*, 2002] and El Junco, Galapagos [*Conroy et al.*, 2008]. (c) Cold tongue δ^{18}O variance from individual *G. ruber* (open circles) as in Figure 3. Error bars indicate the standard error of the variance $\sigma^2\sqrt{(2/(N-1))}$, where σ is the standard deviation and N the sample size. Mar–Sep insolation contrast on the equator is shown in red [*Berger and Loutre*, 1991]. (d) Zonal SST gradient between the west and east Pacific from Mg/Ca (see also Figure 6b). (e) Meridional gradient of the EEP from *G. ruber* δ^{18}O (see also Figure 5).
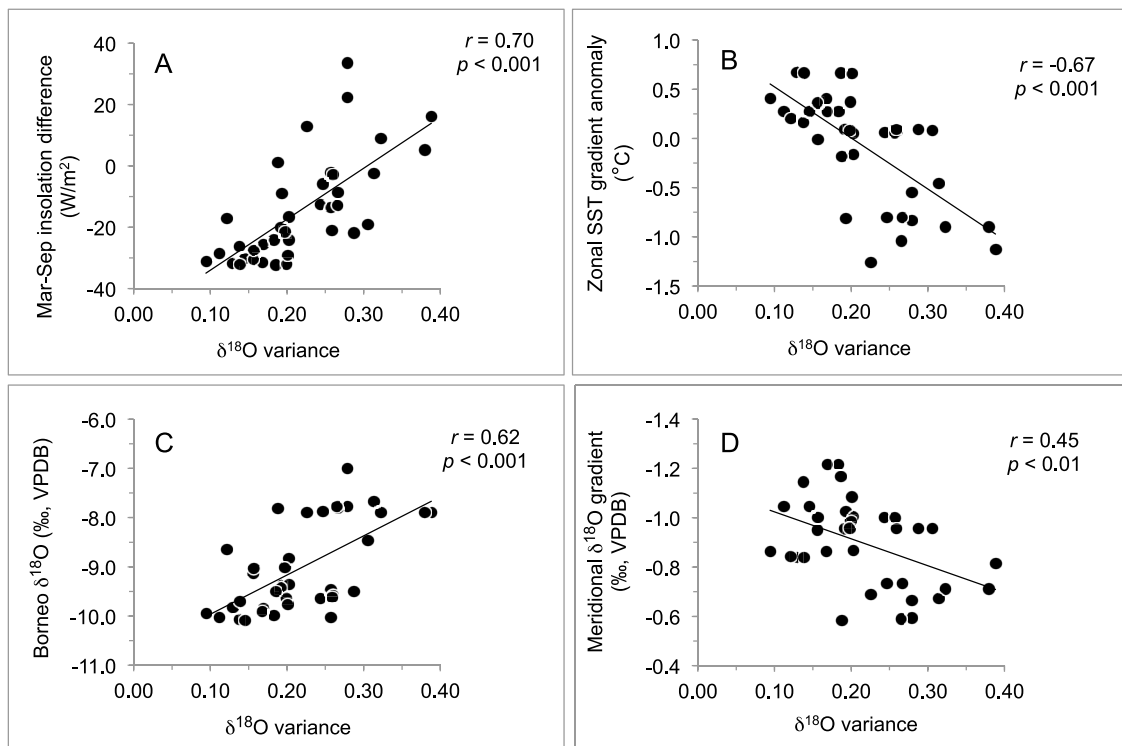
Figure 8. Correlations between *G. ruber* δ^{18}O variance and (a) Mar–Sep insolation difference on the equator; (b) zonal SST gradient anomaly; (c) Borneo speleothem δ^{18}O; (d) meridional δ^{18}O gradient of the EEP. The gradient and Borneo δ^{18}O data are 500-year averages.

References

An, S.-I., A. Timmermann, L. Bejarano, F.-F. Jin, F. Justino, Z. Liu, and A. W. Tudhope (2004), Modeling evidence for enhanced El Niño–Southern Oscillation amplitude during the Last Glacial Maximum, *Paleoceanography*, *19*, PA4009, doi:10.1029/2004PA001020.

Anand, P., H. Elderfield, and M. H. Conte (2003), Calibration of Mg/Ca thermometry in planktonic foraminifera from a sediment trap time series, *Paleoceanography*, *18*(2), 1050, doi:10.1029/2002PA000846.

Bacon, S. N., R. M. Burke, S. K. Pezzopane, and A. S. Jayko (2006), Last glacial maximum and Holocene lake levels of Owens Lake, eastern California, USA, *Quat. Sci. Rev.*, *25*, 1264–1282, doi:10.1016/j.quascirev.2005.10.014.

Bemis, B. E., H. J. Spero, J. Bijma, and D. W. Lea (1998), Reevaluation of the oxygen isotopic composition of planktonic foraminifera: Experimental results and revised paleotemperature equations, *Paleoceanography*, *13*, 150–160, doi:10.1029/98PA00070.

Benson, L., M. Kashgarian, R. Rye, S. Lund, F. Paillet, J. Smoot, C. Kester, S. Mensing, D. Meko, and S. Lindström (2002), Holocene multidecadal and multicentennial droughts affecting northern California and Nevada, *Quat. Sci. Rev.*, *21*, 659–682, doi:10.1016/S0277-3791(01)00048-8.

Benway, H. M., A. C. Mix, B. A. Haley, and G. P. Klinkhammer (2006), Eastern Pacific warm pool paleosalinity and climate variability: 0–30 kyr, *Paleoceanography*, *21*, PA3008, doi:10.1029/2005PA001208.

Berger, A., and M. F. Loutre (1991), Insolation values for the climate of the last 10 million years, *Quat. Sci. Rev.*, *10*, 297–317, doi:10.1016/0277-3791(91)90033-Q.

Bijma, J., W. W. Faber Jr., and C. Hemleben (1990), Temperature and salinity limits for growth and survival of some planktonic foraminifers in laboratory cultures, *J. Foraminiferal Res.*, *20*, 95–116, doi:10.2113/gsjfr.20.2.95.

Bjerknes, J. (1969), Atmospheric teleconnections from the equatorial Pacific, *Mon. Weather Rev.*, *97*, 163–172, doi:10.1175/1520-0493(1969)097<0163:ATFTEP>2.3.CO;2.

Bolliet, T., A. Holbourn, W. Kuhnt, C. Laj, C. Kissel, L. Beaufort, M. Kienast, N. Andersen, and D. Garbe-Schönberg (2011), Mindanao Dome variability over the last 160 kyr: Episodic glacial cooling of the West Pacific Warm Pool, *Paleoceanography*, *26*, PA1208, doi:10.1029/2010PA001966.

Cane, M. A. (2005), The evolution of El Niño, past and future, *Earth Planet. Sci. Lett.*, *230*, 227–240, doi:10.1016/j.epsl.2004.12.003.

Carton, J. A., and B. A. Giese (2008), A reanalysis of ocean climate using Simple Ocean Data Assimilation (SODA), *Mon. Weather Rev.*, *136*, 2999–3017, doi:10.1175/2007MWR1978.1.

Chiang, J. C. H., and C. M. Bitz (2005), Influence of high latitude ice cover on the marine Intertropical Convergence Zone, *Clim. Dyn.*, *25*, 477–496, doi:10.1007/s00382-005-0040-5.

Clement, A. C., R. Seager, M. A. Cane, and S. E. Zebiak (1996), An ocean dynamical thermostat, *J. Clim.*, *9*, 2190–2196, doi:10.1175/1520-0442(1996)009<2190:AODT>2.0.CO;2.

Clement, A. C., R. Seager, and M. A. Cane (2000), Suppression of El Niño during the mid-Holocene by changes in the Earth's orbit, *Paleoceanography*, *15*, 731–737, doi:10.1029/1999PA000466.

Cobb, K. M., C. D. Charles, H. Cheng, and R. L. Edwards (2003), El Niño/Southern Oscillation and tropical Pacific climate during the last millennium, *Nature*, *424*, 271–276, doi:10.1038/nature01779.

Collins, M., et al. (2010), The impact of global warming on the tropical Pacific Ocean and El Niño, *Nat. Geosci.*, *3*, 391–397, doi:10.1038/ngeo868.

Conroy, J. L., J. T. Overpeck, J. E. Cole, T. M. Shanahan, and M. Steinitz-Kannan (2008), Holocene changes in eastern tropical Pacific climate inferred from a Galápagos lake sediment record, *Quat. Sci. Rev.*, *27*, 1166–1180, doi:10.1016/j.quascirev.2008.02.015.

Conte, M. H., M.-A. Sicre, C. Rühlemann, J. C. Weber, S. Schulte, D. Schultz-Bull, and T. Blanz (2006), Global temperature calibration of alkenone unsaturation index ($U_{37}^{K'}$) in surface waters and comparison with surface sediments, *Geochem. Geophys. Geosyst.*, *7*, Q02005, doi:10.1029/2005GC001054.

Dekens, P., D. W. Lea, D. K. Pak, and H. J. Spero (2002), Core top calibration of Mg/Ca in tropical foraminifera: Refining paleotemperature

estimation, *Geochem. Geophys. Geosyst.*, *3*(4), 1022, doi:10.1029/2001GC000200.

DiNezio, P. N., A. Clement, G. A. Vecchi, B. Soden, A. J. Broccoli, B. L. Otto-Bliesner, and P. Braconnot (2011), The response of the Walker circulation to Last Glacial Maximum forcing: Implications for detection in proxies, *Paleoceanography*, *26*, PA3217, doi:10.1029/2010PA002083.

Dubois, N., M. Kienast, C. Normandeau, and T. Herbert (2009), Eastern equatorial Pacific cold tongue during the Last Glacial Maximum as seen from alkenone paleothermometry, *Paleoceanography*, *24*, PA4207, doi:10.1029/2009PA001781.

Fairbanks, R. G., M. Sverdlove, R. Free, P. H. Wiebe, and A. W. Bé (1982), Vertical distribution and isotopic fractionation of living planktonic foraminifera from the Panama Basin, *Nature*, *298*, 841–844, doi:10.1038/298841a0.

Fairbanks, R. G., R. A. Mortlock, T.-C. Chiu, L. Cao, A. Kaplan, T. P. Guilderson, T. W. Fairbanks, A. L. Bloom, P. M. Grootes, and M.-J. Nadeau (2005), Radiocarbon calibration curve spanning 0 to 50,000 years BP based on paired ^{230}Th/^{234}U/^{230}U and ^{14}C dates on pristine corals, *Quat. Sci. Rev.*, *24*, 1781–1796, doi:10.1016/j.quascirev.2005.04.007.

Fedorov, A. V., and S. G. Philander (2001), A stability analysis of tropical ocean–atmosphere interactions: Bridging measurements and theory for El Niño, *J. Clim.*, *14*, 3086–3101, doi:10.1175/1520-0442(2001)014<3086:ASAOTO>2.0.CO;2.

Guilyardi, E., A. Wittenberg, A. Fedorov, M. Collins, C. Wang, A. Capotondi, and G. J. van Oldenborgh (2009), Understanding El Niño in ocean-atmosphere general circulation models: Progress and challenges, *Bull. Am. Meteorol. Soc.*, *90*, 325–340, doi:10.1175/2008BAMS2387.1.

Haug, G. H., K. A. Hughen, D. M. Sigman, L. C. Peterson, and U. Röhl (2001), Southward migration of the Intertropical Convergence Zone through the Holocene, *Science*, *293*, 1304–1308, doi:10.1126/science.1059725.

Karnauskas, K. B., J. E. Smerdon, R. Seager, and J. F. González-Rouco (2012), A Pacific centennial oscillation predicted by coupled GCMs, *J. Clim.*, *25*, 5943–5961, doi:10.1175/JCLI-D-11-00421.1.

Kienast, M., S. S. Kienast, S. E. Calvert, T. I. Eglinton, G. Mollenhauer, R. François, and A. C. Mix (2006), Eastern Pacific cooling and Atlantic overturning circulation during the last deglaciation, *Nature*, *443*, 846–849, doi:10.1038/nature05222.

Koutavas, A., and J. Lynch-Stieglitz (2003), Glacial-interglacial dynamics of the eastern equatorial Pacific cold tongue-Intertropical Convergence Zone system reconstructed from oxygen isotope records, *Paleoceanography*, *18*(4), 1089, doi:10.1029/2003PA000894.

Koutavas, A., and J. P. Sachs (2008), Northern timing of deglaciation in the eastern equatorial Pacific from alkenone paleothermometry, *Paleoceanography*, *23*, PA4205, doi:10.1029/2008PA001593.

Koutavas, A., J. Lynch-Stieglitz, T. M. Marchitto Jr., and J. P. Sachs (2002), El Niño-like pattern in ice age tropical Pacific sea surface temperature, *Science*, *297*, 226–230, doi:10.1126/science.1072376.

Koutavas, A., P. B. deMenocal, G. C. Olive, and J. Lynch-Stieglitz (2006), Mid-Holocene El Niño–Southern Oscillation (ENSO) attenuation revealed by individual foraminifera in eastern tropical Pacific sediments, *Geology*, *34*, 993–996, doi:10.1130/G22810A.1.

Lea, D. W., D. K. Pak, and H. J. Spero (2000), Climate impact of late Quaternary equatorial Pacific sea surface temperature variations, *Science*, *289*, 1719–1724, doi:10.1126/science.289.5485.1719.

Lea, D. W., D. K. Pak, C. L. Belanger, H. J. Spero, M. A. Hall, and N. J. Shackleton (2006), Paleoclimate history of Galápagos surface waters over the last 135,000 years, *Quat. Sci. Rev.*, *25*, 1152–1167, doi:10.1016/j.quascirev.2005.11.010.

Leduc, G., L. Vidal, K. Tachikawa, F. Rostek, C. Sonzogni, L. Beaufort, and E. Bard (2007), Moisture transport across Central America as a positive feedback on abrupt climatic changes, *Nature*, *445*, 908–911, doi:10.1038/nature05578.

Leduc, G., L. Vidal, O. Cartapanis, and E. Bard (2009), Modes of eastern equatorial Pacific thermocline variability: Implications for ENSO dynamics over the last glacial period, *Paleoceanography*, *24*, PA3202, doi:10.1029/2008PA001701.

Levi, C., L. Labeyrie, F. Bassinot, F. Guichard, E. Cortijo, C. Waelbroeck, N. Caillon, J. Duprat, T. de Garidel-Thoron, and H. Elderfield (2007), Low-latitude hydrological cycle and rapid climate changes during the last deglaciation, *Geochem. Geophys. Geosyst.*, *8*, Q05N12, doi:10.1029/2006GC001514.

Locarnini, R. A., A. V. Mishonov, J. I. Antonov, T. P. Boyer, and H. E. Garcia (2006), *World Ocean Atlas 2005*, vol. 1, *Temperature*, *NOAA Atlas NESDIS*, vol. 61, edited by S. Levitus, 182 pp., NOAA, Silver Spring, Md.

Marchitto, T. M., R. Muscheler, J. D. Ortiz, J. D. Carriquiry, and A. van Geen (2010), Dynamical response of the tropical Pacific Ocean to solar forcing during the early Holocene, *Science*, *330*, 1378–1381, doi:10.1126/science.1194887.

McGregor, H. V., and M. K. Gagan (2004), Western Pacific coral δ^{18}O records of anomalous Holocene variability in the El Niño–Southern Oscillation, *Geophys. Res. Lett.*, *31*, L11204, doi:10.1029/2004GL019972.

McPhaden, M. J., S. Zebiak, and N. H. Glantz (2006), ENSO as an integrating concept in Earth Science, *Science*, *314*, 1740–1745, doi:10.1126/science.1132588.

Moy, C. M., G. O. Seltzer, D. T. Rodbell, and D. M. Anderson (2002), Variability of El Niño/Southern Oscillation activity at millennial time-scales during the Holocene epoch, *Nature*, *420*, 162–165, doi:10.1038/nature01194.

Otto-Bliesner, B. L., E. C. Brady, S.-I. Shin, Z. Liu, and C. Shields (2003), Modeling El Niño and its tropical teleconnections during the last glacial-interglacial cycle, *Geophys. Res. Lett.*, *30*(23), 2198, doi:10.1029/2003GL018553.

Partin, J. W., K. M. Cobb, J. F. Adkins, B. Clark, and D. P. Fernandez (2007), Millennial-scale trends in west Pacific warm pool hydrology since the Last Glacial Maximum, *Nature*, *449*, 452–455, doi:10.1038/nature06164.

Pena, L., I. Cacho, P. Ferretti, and M. A. Hall (2008), El Niño–Southern Oscillation–like variability during glacial terminations and interlatitudinal teleconnections, *Paleoceanography*, *23*, PA3101, doi:10.1029/2008PA001620.

Rincón-Martínez, D., F. Lamy, S. Contreras, G. Leduc, E. Bard, C. Saukel, T. Blanz, A. Mackensen, and R. Tiedemann (2010), More humid interglacials in Ecuador during the past 500 kyr linked to latitudinal shifts of the equatorial front and the Intertropical Convergence Zone in the eastern tropical Pacific, *Paleoceanography*, *25*, PA2210, doi:10.1029/2009PA001868.

Rosenthal, Y., D. W. Oppo, and B. K. Linsley (2003), The amplitude and phasing of climate change during the last deglaciation in the Sulu Sea, western equatorial Pacific, *Geophys. Res. Lett.*, *30*(8), 1428, doi:10.1029/2002GL016612.

Shuman, B., A. K. Henderson, S. M. Colman, J. R. Stone, S. C. Fritz, L. R. Stevens, M. J. Power, and C. Whitlock (2009), Holocene lake-level trends in the Rocky Mountains, U.S.A, *Quat. Sci. Rev.*, *28*, 1861–1879, doi:10.1016/j.quascirev.2009.03.003.

Spero, H. J. (1998), Life history and stable isotope geochemistry of planktonic foraminifera, in *Isotope Paleobiology and Paleoecology*, edited by R. D. Norris and R. M. Corfield, *Paleontol. Soc. Pap.*, *4*, 7–36.

Spero, H. J., and D. W. Lea (2002), The cause of carbon isotope minimum events on glacial terminations, *Science*, *296*, 522–525, doi:10.1126/science.1069401.

Spero, H. J., K. M. Mielke, E. M. Kalve, D. W. Lea, and D. K. Pak (2003), Multispecies approach to reconstructing eastern equatorial Pacific thermocline hydrography during the past 360 kyr, *Paleoceanography*, *18*(1), 1022, doi:10.1029/2002PA000814.

Stott, L., C. Poulsen, S. Lund, and R. Thunell (2002), Super ENSO and global climate oscillations at millennial time scales, *Science*, *297*, 222–226, doi:10.1126/science.1071627.

Stott, L., J. Southon, A. Timmermann, and A. Koutavas (2009), Radiocarbon age anomaly at intermediate water depth in the Pacific Ocean during the last deglaciation, *Paleoceanography*, *24*, PA2223, doi:10.1029/2008PA001690.

Stuiver, M., and P. J. Reimer (1993), Extended ^{14}C database and revised CALIB radiocarbon calibration program, *Radiocarbon*, *35*, 215–230.

Timmermann, A., S. J. Lorenz, S.-I. An, A. Clement, and S.-P. Xie (2007), The effect of orbital forcing on the mean climate and variability of the tropical Pacific, *J. Clim.*, *20*, 4147–4159, doi:10.1175/JCLI4240.1.

Tudhope, A. W., C. P. Chilcott, M. T. McCulloch, E. R. Cook, J. Chappell, R. M. Ellam, D. W. Lea, J. M. Lough, and G. B. Shimmield (2001), Variability in the El Niño-Southern Oscillation through a glacial-interglacial cycle, *Science*, *291*, 1511–1517, doi:10.1126/science.1057969.

Visser, K., R. Thunell, and L. Stott (2003), Magnitude and timing of temperature change in the Indo-Pacific warm pool during deglaciation, *Nature*, *421*, 152–155, doi:10.1038/nature01297.

Waelbroeck, C., L. Labeyrie, E. Michel, J. C. Duplessy, J. F. McManus, K. Lambeck, E. Balbon, and M. Labracherie (2002), Sea-level and deep-water temperature changes derived from benthic foraminifera isotopic records, *Quat. Sci. Rev.*, *21*, 295–305, doi:10.1016/S0277-3791(01)00101-9.

Wang, C., and P. C. Fiedler (2006), ENSO variability and the eastern tropical Pacific: A review, *Prog. Oceanogr.*, *69*, 239–266, doi:10.1016/j.pocean.2006.03.004.

Wolff, C., G. H. Haug, A. Timmermann, J. S. Sinninghe Damsté, A. Brauer, D. M. Sigman, M. A. Cane, and D. Verschuren (2011), Reduced interannual rainfall variability in East Africa during the last ice age, *Science*, *333*, 743–747, doi:10.1126/science.1203724.

Xu, J., A. Holbourn, W. Kuhnt, Z. Jian, and H. Kawamura (2008), Changes in the thermocline structure of the Indonesian outflow during terminations I and II, *Earth Planet. Sci. Lett.*, *273*, 152–162, doi:10.1016/j.epsl.2008.06.029.

Zheng, W., P. Braconnot, E. Guilyardi, U. Merkel, and Y. Yu (2008), ENSO at 6 ka and 21 ka from ocean-atmosphere coupled model simulations, *Clim. Dyn.*, *30*, 745–762, doi:10.1007/s00382-007-0320-3.